Technical Note

In-flight Preliminary Performance of GF-5B/Absorbing Aerosol Sensor

Yongmei Wang , Zhuo Zhang * , Jinghua Mao , Houmao Wang , Entao Shi , Xiaohong Liu , Pengda Li , Jiu Liu

Posted Date: 31 July 2023

doi: 10.20944/preprints202307.2044.v1

Keywords: Absorbing aerosol; Absorbing aerosol index; Astigmatic telescope; Imaging spectrometer; Wavelength drift; Radiometric calibration

Technical Notes

In-flight Preliminary Performance of GF-5B/Absorbing Aerosol Sensor

Yongmei Wang [1,2,3,4], Zhuo Zhang [1,3,4,*], Jinghua Mao [1,3,4], Houmao Wang [1,3,4], Entao Shi [1,3,4], Xiaohong Liu [1,2,3,4,] Pengda Li [1,2,3,4] and Jiu Liu [1,3,4]

[1] Laboratory of space environment exploration, National Space Science Center, Beijing 100190, China
[2] School of Astronomy and Space Science, University of Chinese Academy of Sciences, Beijing 100049, China
[3] Beijing Key Laboratory of Space Environment Exploration, Beijing 100190, China
[4] Key Laboratory of Environmental Space Situation Awareness technology, Beijing 100190, China
* Correspondence: zhangzhuo@nssc.ac.cn

Abstract: The Absorbing Aerosol Sensor (AAS) is carried on the Gao Fen 5B (GF-5B) satellite, which allows for measuring the solar backscatter radiation by the atmosphere in UV-VIS wavelength. AAS is an imaging spectrometer using CCD for capturing both continuous spectrum and the cross-track orientation with a 114° wide swath. The broad field-of-view provides daily global envelopment with a 4 km spatial resolution at the nadir. This paper mainly analyzed the initial working status of the instrument in orbit, including wavelength calibration, radiation calibration, detector performance, and product availability. Preliminary observations indicate that the AAS can monitor the absorbing aerosol like dust, biomass burning, volcano ash, and some pollution aerosol and can identify the aerosol events in China and other regions with high spatial resolution.

Keywords: Absorbing aerosol; Absorbing aerosol index; Astigmatic telescope; Imaging spectrometer; Wavelength drift; Radiometric calibration

1. Introduction

Aerosol is an essential and intricate parameter in climate and atmospheric chemistry. Absorbing aerosol is a type of aerosol, like dust, biomass burning, and volcano ash. The absorbing aerosol index (AAI) describes the absorbing aerosols' elevated levels in the troposphere. It detaches the spectral contrast at two ultraviolet (UV) wavelengths induced by absorbing aerosols from the other impacts, such as the Rayleigh scattering, surface reflectance, gaseous absorption, and aerosol and cloud dispersion [1]. Since the surface albedo of land and ocean in the UV area are smaller than in the visible and near-infrared areas, an appropriate UV radiance is required for aerosol identification over land.

Since 1970, many optical sensors have been utilized for ozone, aerosol, and other trace gases. The successful payloads, such as TMOS (Total Map Ozone Suit) on NIMBUS-7 [2], GOME (Global Ozone Monitoring Instrument) on ERS-2 [3], SCIAMACHY (Scanning Imaging Absorption Spectrometer for Atmospheric CartograpHY) on ENVISAT [4], OMI (Ozone Monitoring Instrument) on the EOS-AURA satellite [5], GOME-2 on Metop series satellite [6,7], OMPS (Ozone Mapping Profiler Suite) on NPP/NPOESS [8], and TROPOMI on Sentinel-5P [9], were employed for ozone monitoring and aerosol retrieval products, involving the whole ozone and some trace gases, AAI, and UV-aerosol optical depth [10-12]. Besides, in China, TOU (Total Ozone Unit) on FY-3 [13,14] and EMI (the Environmental Monitoring Instrument) on GF-5A [15] also has the total of ozone and AAI product with lower resolution. Compared with the mentioned payloads, TROPOMI considerably improves the spatial resolution (7 x 7 km or 3.5 x 5.5km) and measurement uncertainty [16].

Absorbing Aerosol Sensor (AAS) is one of the payloads aboard the GaoFen-5B satellite, which is a UV-VIS spectrograph that integrates high spatial resolution and low spectral resolution with daily global coverage. The origin of air pollution can be analyzed using the high ground pixel projection and considerable temporal resolution. AAS has been employed as the first tool to absorbing aerosol observation by acquiring a continuous spectrum in the 340–550 nm interval in China. The GF-5B Satellite is a sun-synchronous satellite with an orbit height of 705 km and an orbit period of ~101

Preprints (www.preprints.org) | NOT PEER-REVIEWED | Posted: 31 July 2023 doi:10.20944/preprints202307.2044.v1

minutes, and its primary mission is for atmospheric chemistry, including aerosol and high-resolution land observation.GF-5B satellite was launched at 10:30 UTC on September 6, 2021. This paper presents AAS instrumental descriptions and initial observations during the first year in orbit.

This paper includes six sections. Following the introduction in Section 1, the instrument description is introduced in Section 2. Sections 3 and 4 present the calibration on-ground and in orbit, respectively, while assessing the performance in orbit. Section 5 presents the preliminary products. The conclusions and future research perspective are presented in Section 6.

2. Instrument Illustration

AAS is a broad field-of-view (FOV), pushbroom imaging spectrograph employing a two-dimensional detector for realizing the spectral and spatial imaging. The main specifications of AAS are summarized in Table 1.

Table 1. GF-5B/AAS primary optical properties.

Parameter	Characteristics
Spectral range (nm)	338.52-551.85
Spectral resolution (nm)	1.726-1.886nm
FOV	±57°
Spatial resolution	4 km × 4 km (at nadir)
SNR	>1000 (10.89 μW/cm². sr. nm)

The AAS design schematic has been described by Shi et al. [17]. The optical system comprises the telescope, spectrometer, detector, and calibration module. A polarization scrambler is located on the telescope's optical trajectory to reduce the measurement sensitivity to the input radiance's polarization status. The whole optical schematic is shown in Figure 1. The AAS is an anamorphic, astigmatic, reflective, two-concave-mirror, along tracking telecentric, cross-orientation f-theta telescope to guarantee the linearity of the image height to the field angle at swath orientation [18]. Compared with a spherical surface, the telescope's two mirrors have a freeform surface to meet the critical spatial need. Figure 2 describes the telescope's optical system. A 3-dimensional slit was utilized to alleviate the error of the lines' accurate shape in the acquired spectrum [19]. This 3D slit comprised two high reflective plane mirrors and was glued together with two exact spacers at the edges. The telescope and spectrometer focal planes are coupled in the swath direction to maintain a perfect spatial image, while the telescope is concentrated at the SH entrance in the along tracking orientation, and the objective plane of the spectrometer is at its exit.

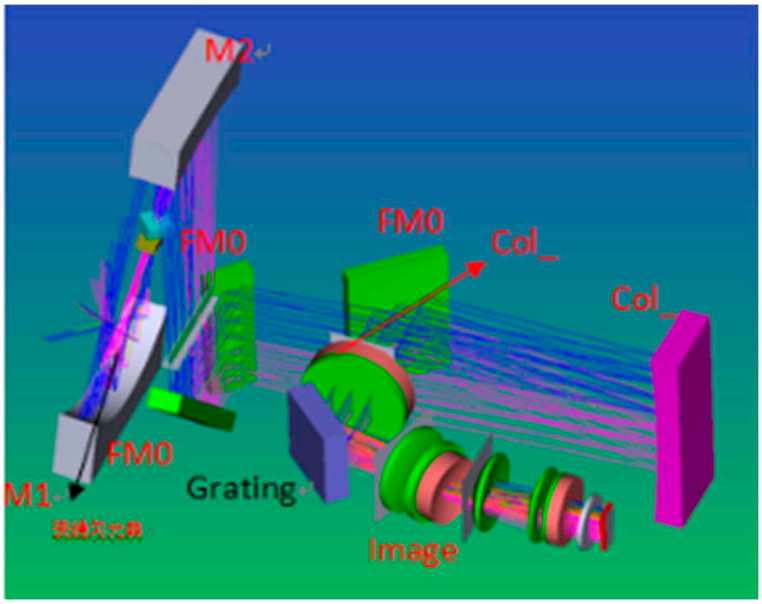

Preprints (www.preprints.org) | NOT PEER-REVIEWED | Posted: 31 July 2023 doi:10.20944/preprints202307.2044.v1

Figure 1. AAS's optical schematic.

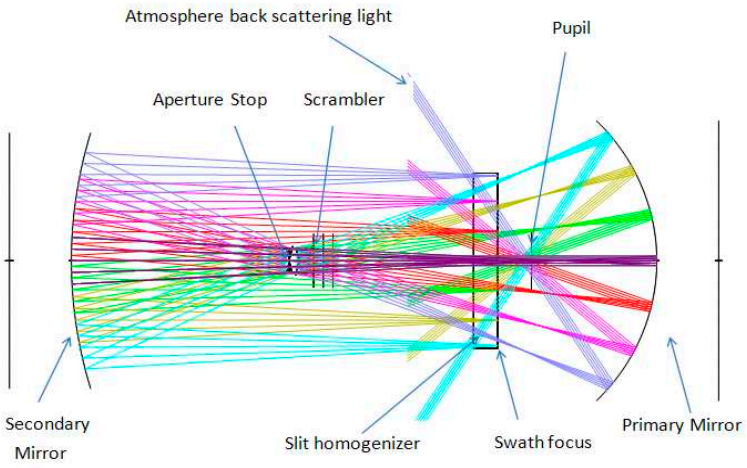

Figure 2. Scheme of the telescope.

The AAS monitors the sun once per 10 days through a quartz diffuser (A1) and the other quartz diffuser (A2) to monitor the diffuser A1 degradation once per 3 months. The radiometric calibration comprises the absolute radiance and irradiance calibrations. The ratio of the two forms the instrument BSDF calibration parameter, indicating the earth reflectance calibration. Figure 3 shows the optical path schematic. The optical pathways for radiance and irradiance channels are the same except for the reflection diffuser that will be moved into the optical pathway during irradiance calibration. As the sun is employed for measurements, the diffuser is located in the calibration position, which will block the earth's radiance and point to solar irradiance. AAS has an internal white light source (WLS) for detector bad pixel identification, employing the same configuration as the irradiance calibration mode. Thus, these calibration schematics are suitable for the calibration and attenuation evaluation of all optical components.

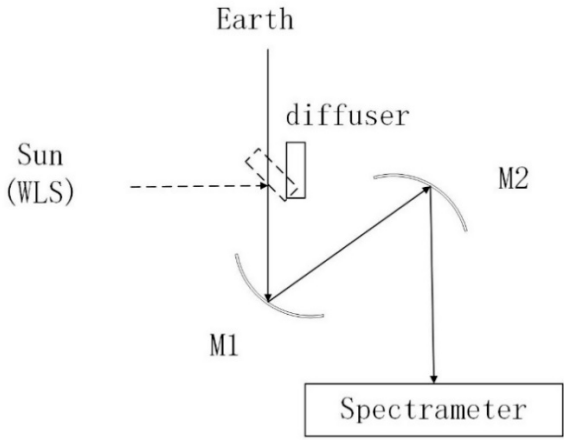

Figure 3. Scheme of in-orbit calibration.

The wavelength calibration is accomplished during the flight using the solar Fraunhofer absorbing line. The AAS is operated in orbit at temperatures of 20 ±2°C for the optical bench and 5±0.5°C for the CCD detector.

3. Calibration on Ground

Preprints (www.preprints.org) | NOT PEER-REVIEWED | Posted: 31 July 2023 doi:10.20944/preprints202307.2044.v1

During the preflight test, the spectral characteristics include the wavelength calibration and the Instrument Slit Function (ISF). The wavelength calibration has been performed using three spectral line sources, including a mercury (Hg) lamp, argon (Ar) lamp, and a krypton (Kr) lamp. Besides, the ISF has been measured using the dedicated ISRF equipment as an echelle grating spectrometer. The results are shown in Figure 4. A super-Gaussian function was considered for the ISRF of the instrument. It fits with a fourth-order polynomial, thus giving the wavelength value for a predefined CCD pixel and an FWHM of 1.726-1.82 nm for all the wavelength ranges.

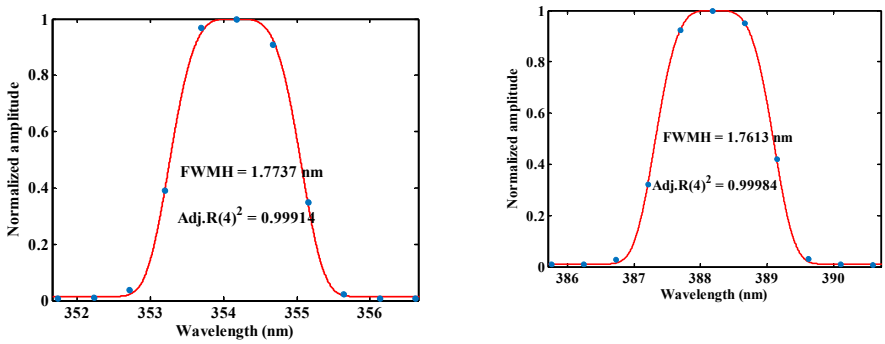

Figure 4. The ISRF for different wavelengths using a dedicated ISRF equipment.

The following formula describes the super-Gaussian profile:

$$y = A_2 + A_1 \cdot \mathrm{e}^{-((\lambda-\lambda_0)./c_0)^4)} \quad (1)$$

where A_1, A_2, λ_0, and c_0 are the fitting parameters.

The AAS instrument's radiometric calibration includes the radiance and irradiance calibration, and the instrument calibration, which can be described with a Bi-directional Spectral Distribution Function (BSDF), equals the irradiance ratio to the radiance calibration coefficient.

The radiance calibration is related to the cross-track angle and wavelength. Therefore, radiance calibration for the AAS instrument is performed in three steps. First, the total FOV of 114 degrees at ambient environmental conditions is divided into 12 small FOVs for testing, then jointing to the full field radiance calibration. Second, absolute radiance calibration at nadir is completed under a vacuum environment and the operating temperature in orbit. Lastly, the radiance calibration coefficient for full FOV under a vacuum environment is obtained by interpolation fitting using the results of the first two steps.

The irradiance calibration is related to the wavelength, solar elevation, and azimuth angles. The elevation angle varies when the satellite moves in orbit from –4.0° to +4.0° with a nominal value of 0.0°. The azimuth angle varies with season between 25.7°± 11.5°. The BSDF is related to the swath angle, elevation and azimuth angles, diffuser, and wavelength. As shown in Figure 5, BSDF varies from 0.3 to 0.35 at an elevation angle value of 0 °and azimuth angle value of 25.7°depending on wavelength. The central FOV value of BSDF is 0.321. There is much less variation in wavelength, which is compatible with the diffuser characteristics.

Preprints (www.preprints.org) | NOT PEER-REVIEWED | Posted: 31 July 2023 doi:10.20944/preprints202307.2044.v1

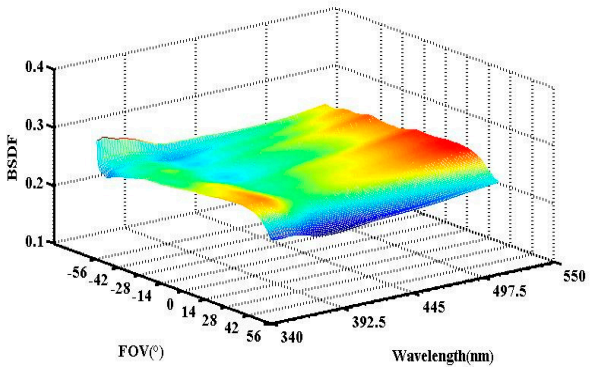

Figure 5. The BSDF of the diffuser (elevation angle of 0 and azimuth angle of 25.7°).

4. Calibration in Orbit

Solar irradiance, spectral calibration, dark background, and WLS measurements can be analyzed on the calibration mode in orbit.

4.1. Wavelength Drift

The wavelength assignment in orbit is performed through fitting a reference solar spectrum [20,21]. The standard solar spectrum is from SAO 2010. The wavelength calibration includes confirmation of wavelength calibration equations, spectral resolution, and calibration accuracy. Solar Fraunhofer lines are employed to perform spectral registration. First, the Fraunhofer line peak position matching is considered. The polynomial fitting is then employed to calculate the spectral calibration equation to obtain the corresponding wavelength for a given CCD pixel and the instrument's spectral range.

For the spectral resolution, the high-resolution reference solar spectrum will be convoluted with the AAS instrument spectral response function, and simulates the spectral curve with different spectral resolutions, compared with the observed spectrum of AAS. When the spectral residual meets the threshold, the spectral resolution for AAS can be confirmed.

According to the AAS instrument characteristics, nine solar Fraunhofer lines can be selected, 7 of which are employed for wavelength equation calculation, and the other two are utilized to evaluate wavelength calibration accuracy.

The spectral calibration data is based on AAS's 471 orbit solar calibration data on October 9, 2021. The spectral band of AAS was obtained in the range of 338.3-551.5 nm, its spectral resolution was between 1.726 nm and 1.82 nm, and the spectral calibration accuracy was less than 0.09 nm.

The temperature control system works well during the orbital operation. The temperature of the spectrometer is 20±1.0°C, and the detector's working temperature is 5±0.4°C. According to the wavelength monitoring results for more than nine months in orbit, the maximum wavelength drift of AAS is below 0.039 nm, less than 1/39 of the spectral resolution, indicating no significant wavelength drift since launching. The result is shown in Figure 6.

Preprints (www.preprints.org) | NOT PEER-REVIEWED | Posted: 31 July 2023 doi:10.20944/preprints202307.2044.v1

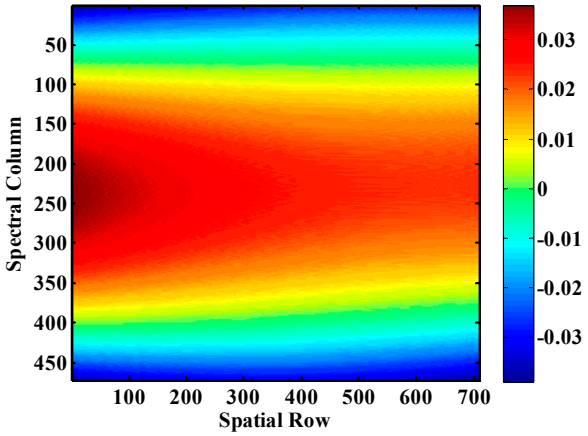

Figure 6. The wavelength drift for AAS since launching (Unit: nm).

4.2. Radiometric Calibration and Stability

Figure 7 compares the AAS on 09 October 2021 (orbit 471) and the reference solar spectrum. An improved high-resolution reference solar spectrum (SAO 2010) was utilized [20]. Due to the lower spectral resolution of AAS, the reference solar spectrum was convolved with the AAS spectral slit function. Although the fine structure could not be found in Figure 7, some solar Fraunhofer characteristic lines could be identified, which could be employed for the wavelength calibration in orbit. The maximum deviation between the solar spectrum measured by AAS and the reference solar spectrum is 3.82%. After launching more than 290 days, the solar irradiance at all wavelengths does not decrease significantly, indicating no evident performance degradation of the AAS, which should be analyzed in future.

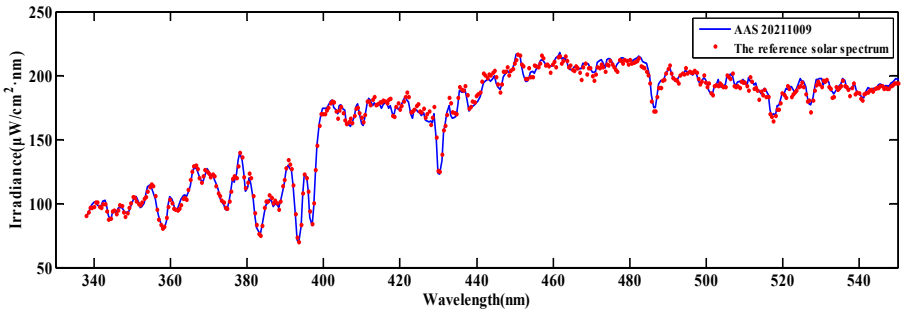

Figure 7. Comparing the measured solar spectrum over the diffuser (A1) by AAS (orbit 0471, 09 October 2021) with the reference solar spectrum SAO2010, which is convolved with the AAS slit function.

After launching, the WLS monitoring mode was utilized to verify the AAS instrument's in-orbit radiometric stability and the CCD performance during flight. The WLS mode is operated once per 10 days, and the WLS is lighted 5 minutes per time. Figure 8 describes the relative radiometric stability at all wavelengths versus time. For any date, the signal acquired from the WLS measurement is divided by that acquired from the first measurement on 23 September 2021. The results indicate that the signal variation with wavelength is slow, with a more evident trend in a shorter wavelength, where the maximum is about 3.8% after 290 days in orbit. This phenomenon may be related to the increase in lighting time, stimulating the halogen efficiency of the WLS bulb to enhance the WLS throughput.

Preprints (www.preprints.org) | NOT PEER-REVIEWED | Posted: 31 July 2023 doi:10.20944/preprints202307.2044.v1

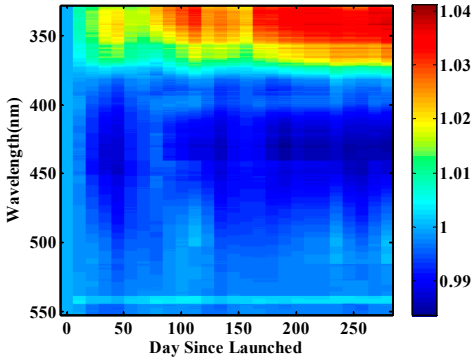

Figure 8. The relative variation of the WSL monitoring with all wavelengths, normalized with the measurement on 23 September 2021.

4.3. Dark Noise

In the space environment, high-energy particles will affect the detector's dark current. Special shielding protection has been taken to design the detector and the control circuit. During the in-orbit operation, the dark background measurement performed by each orbit when the satellite enters the shadow area and the analysis of the dark current noise level can evaluate the detector's capability to resist space radiation environment, which is also very crucial to understand the operational status of the instrument and data retrieval. Figure 9 gives the dark background noise variation since AAS was switched on. According to the detector's temperature monitoring, the detector's working temperature is stable in the range of 5±0.4°C. The dark noise is stable between 1.77-2.26 DN (rms) after AAS has been in orbit for more than nine months, indicating the stable operating state of the detector assembly. There is no evident influence from the space radiation environment.

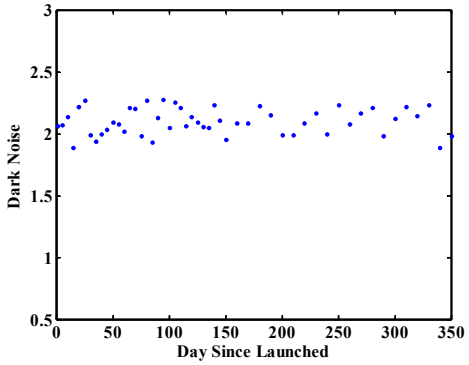

Figure 9. Dark Noise trend in orbit.

5. Product Availability and Examples

Like trace gases in the atmosphere, aerosol particles have scattering and absorption characteristics in UV and visible bands. UV absorbing aerosol index (AAI) utilizes the absorption differences between the two bands to monitor pollution aerosols (such as dust storms, haze, black carbon, and volcanic ash clouds) [22,23]. In previous work, the Absorbing Aerosol Index has been studied based on the observation data of FY-3B/TOU combined with the simulation results [24,25], and our AAI inversion algorithm was established to obtain the preliminary observation results. The AAS will monitor the absorbing aerosols in a large area with high spatial resolution.

During the commissioning phase, the retrieved result of AAS was compared with the SENTINEL-5P/TROPOMI operational products (https://s5phub.copernicus.eu/dhus/#/home). Figure 10(a, b) shows the AAI distribution for both payloads in the Taklamakan Desert and nearby regions on March 25th, 2022. After spatial image matching (Figure 10(c, d)), the AAI was statistically analyzed

Preprints (www.preprints.org) | NOT PEER-REVIEWED | Posted: 31 July 2023 doi:10.20944/preprints202307.2044.v1

to obtain the correlation coefficient *R* of 0.784 between the two payloads (Figure 10e) with 6615 pairs of samples. In Figures 10c and d, the results in (a) and (b) have been projected into 0.08°×0.08° grids, and the data in the same grid has been averaged into one value. The orbital temporal difference between GF-5B (descending node) and SENTINEL-5P satellite (ascending node) is about 3 hours. The relative deviation of retrieval results is reasonable considering the difference in atmospheric variation and geometric conditions. Therefore, the AAI by AAS deviates from the AAI by TROPOMI. However, there is a high consistency between the two from the perspective of qualitative analysis of aerosol pollution, preliminarily demonstrating the availability of AAS products.

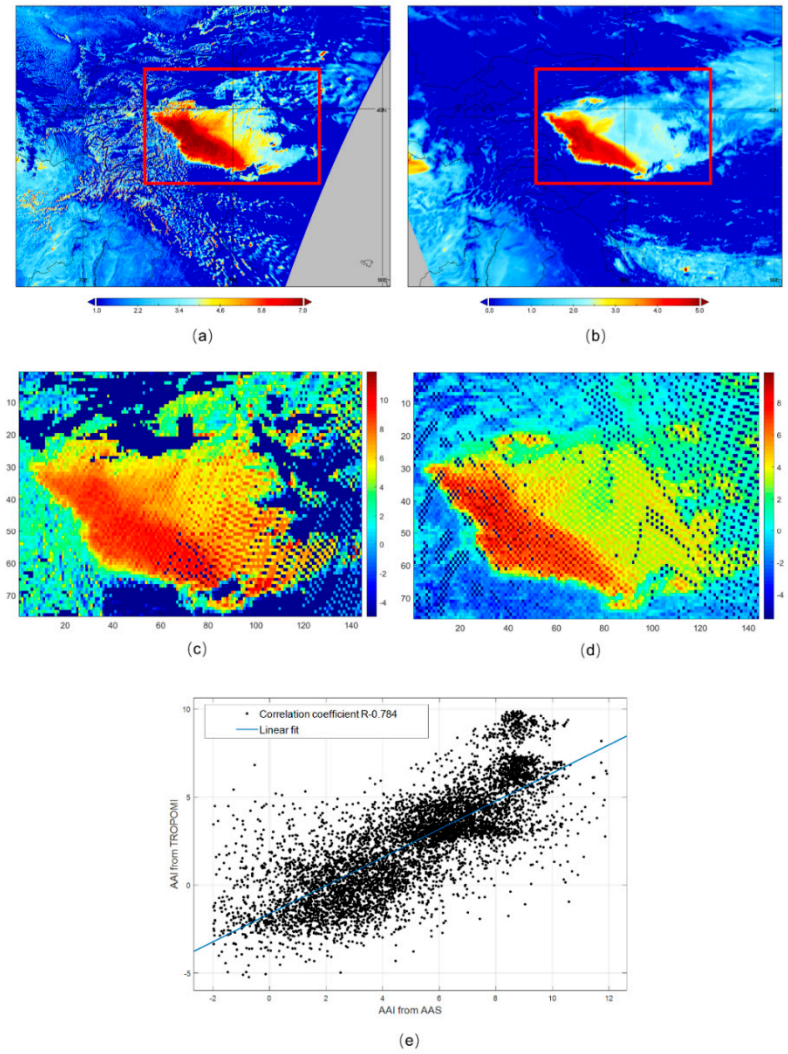

Figure 10. The correlation analysis of AAI in the Taklimakan Desert region between AAS and TROPOMI (25th March 2022). AAI of AAS (a); AAI of TROPOMI (b); 0.08°×0.08° grid average for AAS (c); 0.08°×0.08° grid average for TROPOMI (d); The correlation coefficient *R* of AAI in the Taklimakan Desert region between AAS and TROPOMI (25th March 2022) is 0.784 with 6615 pairs of samples.

Aerosol pollution in the Chinese region is significantly associated with the eastward movement of dust storms in western China. On April 21st 2022, AAS monitored a high concentration of absorbing aerosols over Xinjiang, Qinghai, Gansu, Inner Mongolia, North China, and Northeast China, indicating large-scale air pollution (Figure 11a). PM10 concentrations from the ground-based air quality monitoring network (https://www.aqistudy.cn/#) exhibited high values in the above regions (Figure 11b), with southern Xinjiang and parts of North China even exceeding 500 μg/m^3, which is a severe aerosol pollution event. It indicates the compatibility of the dust area characterized by the AAI

Preprints (www.preprints.org) | NOT PEER-REVIEWED | Posted: 31 July 2023 doi:10.20944/preprints202307.2044.v1

detected by AAS with the ground-based PM10 monitoring results. Besides, the dust storm moving and spreading from west to east can be monitored. Since the spatial resolution of the current AAS inversion product is 2×4km, the dust aerosol's spatial distribution features in various areas can be clearly distinguished from the regional AAI distribution map from north to northeast China (Figure 11a), which indicates that AAS can provide a higher identification capability of aerosol local distribution characteristics in critical areas with high spatial resolution.

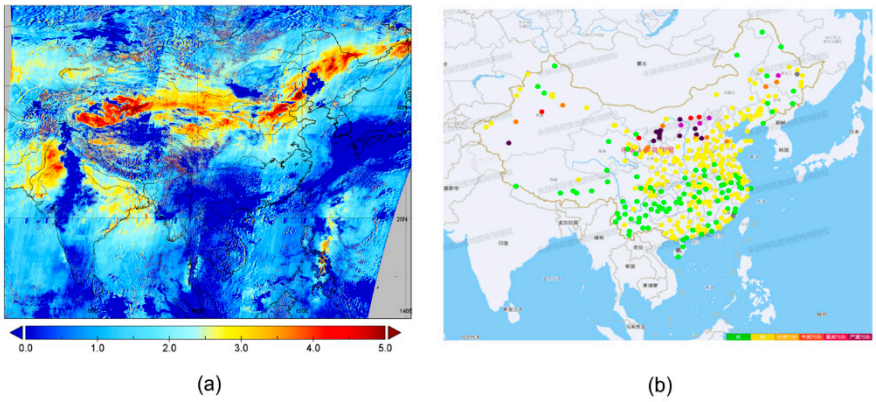

Figure 11. Absorbing Aerosol monitored in China (20220421) by (a) AAS; (b) PM10 at 11 am from the AQI China website.

Figure 12 shows the global distribution of AAI observed by AAS on April 11, 2023. It plays an essential role in the dust observation in China [26] and pollutants in Southeast Asia in the spring of 2023. Figure 12 describes the distribution of sand and dust pollutants in China and the impact of incineration pollutants in Southeast Asia on surrounding areas. The dust pollution in North China has been transported from the Taklimakan Desert to the northeast and has spread to the south to cover the Shandong Peninsula. Pollutants from incineration in Southeast Asia have caused severe pollution in surrounding areas. At the same time, the Sahara Desert, the Arabian Peninsula, and the Mongolian Plateau have a large area of dust distribution.

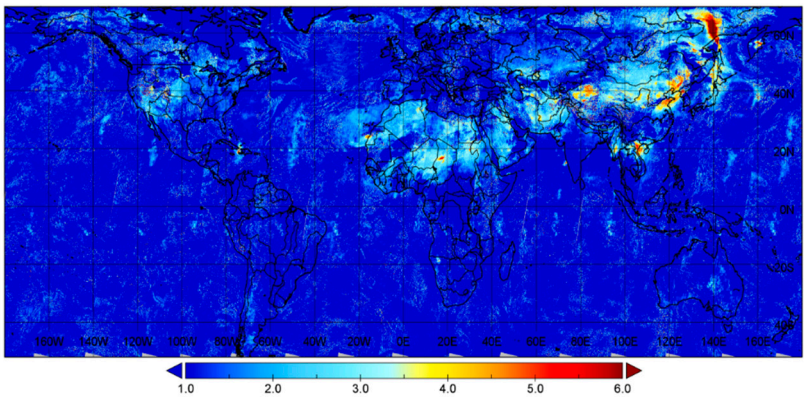

Figure 12. The global distribution of absorbing aerosol by AAS on April 11, 2023.

6. Conclusion

AAS on the GF-5B satellite was launched on September 6, 2021. AAS measures the solar backscatter radiance and solar irradiance in the spectral region from 339nm to 551nm by combining high spatial and low spectral resolutions with daily global envelopment. The mentioned results indicate the radiometric calibration compared with the TROPOMI measurement. The instrument

indicates no optical decay within the wavelength range throughout the first year after launch. The in-flight spectral calibration shows that the maximum wavelength shift is below 0.039nm.

Preliminary observations show that the AAS can identify aerosol pollution, including dust and some severe air pollution cases with high spatial resolution in China. The AAI results of the TROPOMI observation of a highly severe dust pollution event in the Taklimakan Desert on March 25, 2022, were compared with the AAS observation results, while the correlation coefficient R was 0.784. This correlation is reasonable considering that the time difference between the two satellites is about 4 hours, and the specific pixel pollution condition will change slightly. At the same time, analyzing a long-distance dust pollution event in China on April 21, 2022, indicated that the dust distribution between the two areas was the same, and the pollutant distribution results were also compatible with PM10 observed by ground-based instruments. By applying the AAI observed by AAS to the absorbing aerosol distribution observation in spring 2023, we can track the impact of dust pollution in China and incineration pollution in Southeast Asia on the surrounding areas. In summary, the AAI products by AAS can observe and track absorbing aerosol pollutants.

From a future research perspective, more detailed analysis and validation for AAI products should be discussed. As the next step, the aerosol type analysis will be implemented by integrating the AAI with the high-resolution aerosol optical thickness products to better distinguish the absorbing aerosol.

Author Contributions: Writing—original draft preparation Y.W; Instrument optical design, E.S; Instrument structure design, J.L; on-ground calibration, J. H, Y. W and P.L; software, X.L; in orbit calibration, H.W and Y.W; product validation, Z.Z.; writing—review and editing, Z.Z, Y.W and J. H.; All authors have read and agreed to the published version of the manuscript.

Funding: This work was funded by the National Gao-Fen Satellite Office, under the GF-5B/AAS project contract.

Data Availability Statement: The data presented in this study are available on request from the author.

Acknowledgments: The authors wish to thank GF-5B Project team and Guojun Du from Beijing Institute of Space Mechanics & Electricity (BSME), professor Weihe Wang from National Satellite Meteorological Center (CMA), Yuerong Cai and Hao Qiao fromm National Spcae Science Center (NSSC). The authors also thank to NASA for the provisions of TROPOMI, and the Air quality monitoring database for providing the reliable ground-based PM10 data.

Conflicts of Interest: The authors declare no conflict of interest.

References

1. Dave, J.V. Effect of aerosols on the estimation of total ozone in an atmospheric column from the measurements of its ultraviolet radiance. *J. Atmos. Sci.* **1978**, *35*, 899-911.
2. McPeters, R.D.; Bhartia, P.K.; Arlin, J.K.; Herman, J.R.; Wellemeyer, C.G.; Seftor, C.J.; Jaross, G.; Torres, O.; Moy, L.; Labow, G.; et al. Earth Probe Total Ozone Mapping Spectrometer (TOMS) Data Products User's Guide. NASA Technical Publication: Washington, USA, 1998.
3. Hahne, A.; Lefebvre, A.; Callies, J. Global ozone monitoring experiment (GOME) on board of ERS 2. In Environmental Sensing '92, Berlin, Germany, 15-19 June 1992.
4. Bovensmann, H.; Burrows, J.P.; Buchwitz, M.; Frerick, J.; Noël, S.; Rozanov, V.V.; Chance, K.V.; Goede, A.P.H. SCIAMACHY: Mission objectives and measurement modes. J. Atmos. Sci. **1999**, *56*, 127-150.
5. De Vries, J.; van den Oord, G.H.J.; Hilsenrath, E.; te Plate, M.B.J.; Levelt, P.F.; Dirksen, R. Ozone monitoring instrument (OMI). In International Symposium on Optical Science and Technology, San Diego, CA, United States, 29 July - 3 August 2001.
6. Callies, J.; Corpaccioli, E.; Eisinger, M.; Hahne, A.; Lefebvre, A. GOME-2 – metop's second-generation sensor for operational ozone monitoring. Available online: https://www.esa.int/esapub/bulletin/bullet102/Callies102.pdf (accessed on May 2000).
7. Munro, R.; Lang, R.; Klaes, D.; Poli, G.; Retscher, C.; Lindstrot, R.; Huckle, R.; Lacan, A.; Grzegorski, M.; Holdak, A.; et al. The GOME2 instrument on the Metop series of satellites: Instrument design, calibration, and level 1 data processing – an overview. *Atmos. Meas. Tech.* **2016**, *9*, 1279-1301.
8. Seftor, C.J.; Jaross, G.; Kowitt, M.; Haken, M.; Li, J.; Flynn, L.E. Post launch performance of the Suomi National Polar-orbiting Partnership Ozone Mapping and Profiler Suite (OMPS) nadir sensors. *J. Geophys. Res. Atmos.* **2014**, *119*, 4413-4428.
9. Veefkind, J.P.; Aben, I.; McMullan, K.; Forster, H.; de Vries, J.; Otter, G.; Claas, J.; Eskes, H.J.; de Haan, J.F.; Kleipool, Q.; et al. TROPOMI on the ESA Sentinel-5 Precursor: A GMES mission for global observations of

the atmospheric composition for climate, air quality and ozone layer applications. *Remote Sens. Environ.* **2012**, *120*, 70-83.
10. Torres O.; Tanskanen, A.; Veihelmann B.; Ahn, C.; Braak, R.; Bhartia, P.K.; Veefkind, P.; Levelt, P. Aerosols and surface UV products from Ozone Monitoring Instrument observations: An overview. *J. Geophys. Res.* **2007**, *112*, D24S47.
11. Levelt, P.F.; Hilsenrath, E.; Leppelmeier, G.W.; van den Oord, G.H.J.; Bhartia, P.K.; Tamminen, J.; de Haan, J.F.; Veefk, J.P. Science objectives of the ozone monitoring instrument. *IEEE Trans. Geosci. Remote Sens.* **2006**, *44*, 1199-1208,
12. Kooreman, M.L.; Stammes, P.; Trees, V.J.H.; Sneep, M.; Tilstra, L.G.; de Graaf, M.; Stein Zweers, D.C.; Wang, P.; Tuinder, O.N.E.; Veefkind, J.P. Effects of clouds on the UV Absorbing Aerosol Index from TROPOMI. *Atmos. Meas. Tech.* **2020**, *13*, 6407-6426.
13. Wang, Y.M.; Wang, Y.J.; Wang, W.H.; Zhang, Z.M.; Lu, J.G.; Fu, L.P.; Jiang, F.; Chen, J.; Wang, J.H.; Guan, F.J.; et al. FY-3 satellite ultraviolet total ozone unit. *Chin. Sci. Bull.* **2010**, *55*, 84-89.
14. Wang. W.H.; Zhang X.Y.; Wang Y.M.; Wang Y.J.; Zhang Z.M.; Fu L.P.; Jiang F.; Liu G.Y. Introduction to the FY-3A Total Ozone Unit: Instrument, performance and results. I*nt. J. Remote Sens.* **2011**, *32*, 4749-4758.
15. Tang, F.Y.; Wang, W.H.; Si, F.Q.; Zhou, H.J.; Luo, Y.H.; Qian, Y.Y. Successful derivation of absorbing aerosol index from the environmental trace gases monitoring instrument (EMI). *Remote Sens.* **2022**, *14*, 4105.
16. Ludewig, A.; Kleipool, Q.; Bartstra, R.; Landzaat, R.; Leloux, J.; Loots, E.; Meijering, P.; van der Plas, E.; Rozemeijer, N.; Vonk, F.; et al. In-flight calibration results of the TROPOMI payload on board the Sentinel-5 Precursor satellite. *Atmos. Meas. Tech.* **2020**, *13*, 3561-3580.
17. Shi, E.T.; Wang, Y.M.; Jia, N.; Mao, J.H.; Lu, G.D.; Liang, S.L. Absorbing aerosol sensor on gao-fen 5B satellite. *Adv. Opt. Techn.* **2018**, *7*, 387-393.
18. David Nijkerk, Bart van Venrooy, Peter Van Doorn, Rens Henselmans, Folkert Draaisma, and André Hoogstrate "The TROPOMI Telescope", Proc. SPIE 10564, International Conference on Space Optics — ICSO 2012, 105640Z (20 November 2017); https://doi.org/10.1117/12.2309035
19. Jérôme Caron, Bob Kruizinga, and Rob Vink "Slit homogenizers for Earth observation spectrometers: overview on performance, present and future designs", Proc. SPIE 11180, International Conference on Space Optics — ICSO 2018, 1118012 (12 July 2019); https://doi.org/10.1117/12.2535957
20. Chance, K.; Kurucz, R.L. An improved high-resolution solar reference spectrum for Earth's atmosphere measurements in the ultraviolet, visible, and near infrared. *J. Quant. Spectrosc. Radiat. Transf.* **2010**, *111*, 1289-1295.
21. Van Geffen, J.H.G.M. Wavelength Calibration of spectra measured by the Global Ozone Monitoring Instrument: variation along orbits and in time. *Appl. Optics* **2004**, *43*,695-706.
22. Torres O.; Bhartia, P.K.; Herman, J.R.; Ahmad, Z.; Gleason, J. Derivation of aerosol properties from satellite measurements of backscattered ultraviolet radiation: Theoretical basis. *J. Geophys. Res.* **1998**, *103*, 17099-17110.
23. de Graaf, M.; Stammes, P.; Torres, O.; Koelemeijer, R.B.A. Absorbing aerosol index: sensitivity analysis, application to gome and comparison with toms. *J. Geophys. Res. Atmospheres* **2005**, *110*, 372-384.
24. Zhang, Z.; Wang Y.M.; Wang W.H.; Wang, H.M. Sensitivity study of viewing path and spectral resolution on absorbing aerosol index. *Chinese Journal of Space Science* **2019**, *39*, 93-99. (in Chinese)
25. Zhang, Z.; Wang W.H.; Wang Y.M.; Wang, Y.M. Effects of humidity on absorbing aerosol index. *National Remote Sensing Bulletin* **2019**, *23*, 1177-1185. (in Chinese)
26. Chen, S.Y.; Zhao, D.; Huang J.P.; He, J.Q.; Chen Y.; Chen J.Y.; Bi, H.R.; Lou G.T.; Du, S.K.; Zhang, Y.; et al. Mongolia contributed more than 42% of the dust concentrations in northern china in March and April, 2023. *Adv. Atmos. Sci.* **2023**, *40*, 1549-1557.